Object Detection and Image Reconstruction Using Microwave Technology

Master's thesis in Electrical Engineering

Ben Wish Le

School of Engineering
UNIVERSITY OF CENTRAL OKLAHOMA
State of Oklahoma, U.S.A. 2024

Object Detection and Image Reconstruction Using Microwave Technology

Thesis Title

Ben Wish Le

Author's Name

12/09/2024

Date

Jackson College of Graduate Studies at the University of Central Oklahoma

A THESIS APPROVED FOR

Master of Science in Electrical Engineering

Committee Chairperson

Committee Member

Committee Member

Object Detection and Image Reconstruction Using Microwave Technology

Master's thesis 2024

Ben Wish Le

Object Detection and Image Reconstruction Using Microwave Technology
Printed: Edmond, University of Central Oklahoma

Abstract

Microwave imaging holds significant potential in the medical field, offering advantages over traditional methods like X-rays and MRI. It is both cost-effective and uses non-ionizing radiation, making it a safer option. Although microwave tomography is complex, it shows promise for imaging soft tissues. The longer wavelengths used are more affected by diffraction, meaning that the assumption of straight-line propagation in a dielectric medium is generally valid only at higher frequencies, such as in the ultraviolet or gamma ray range. Using a circular radar aperture for imaging, combined with advanced post-processing reconstruction techniques, can enhance the overall performance of the imaging system. Simulations demonstrate that employing an ultrawide band (UWB) increases depth resolution, while improved angular resolution enhances cross-range accuracy, making it possible to pinpoint the location and range of targets. However, there's a tradeoff between attenuation and resolution that varies with frequency, especially in materials that absorb energy. A stable imaging system is essential for consistent measurements, particularly when removing artifacts. My attempt at reconstructing an image from measured data was semi-successful due to a high margin of phase error, which led to inconsistencies in the results. Future research has substantial potential to improve image reconstruction quality further. MATLAB's extensive library resources make it a valuable tool for advancing these enhancements.

Contents

List of Tables

Preface

Various scanning and imaging systems serve a range of functions, from object detection and positioning to applications in healthcare. Medical imaging uses diverse technologies, including CT, PET, MRI, and ultrasound. Since these methods were first developed, awareness of radiation risks and cost concerns has grown, driving the need for a safer, mobile, and highly accurate imaging solution. Scientists have recognized the potential of microwave imaging, with research focused on refining parts of this technology. However, microwave tomography has faced challenges, such as the high cost of specialized hardware and limited computing power. The goal of this thesis is to help develop an effective imaging system that could be useful in medical diagnostics. Reducing the cost of these systems while maintaining diagnostic capabilities could make healthcare more accessible, particularly in low-income regions.

Breast cancer remains the most frequently diagnosed cancer among women in the United States, accounting for about 30% of all new cancer cases in women each year. In 2024, it's estimated that approximately 310,720 women will receive a diagnosis of invasive breast cancer, with 16% of these cases occurring in women under the age of 50 [50000]. Since treating breast cancer correctly is critical, a fast diagnosis can mean the difference between life-saving care and dangerous complications. Real-time microwave imaging could greatly improve the speed and accuracy of these critical diagnoses, offering repeated assessments as often as needed by the patient.

Acknowledgements

This work is dedicated to my parents, whose love and support have been my foundation and source of motivation.

My deepest gratitude goes to my advisors, Dr. Alsbou and Dr. Ali from The University of Oklahoma Health Sciences Center, for their invaluable guidance and insights, which were instrumental throughout my thesis. Their dedication serves as a true inspiration for the scientist I aspire to become.

I would also like to thank my co-supervisors, Dr. Jiang and Dr. Lemley, for their essential feedback and encouragement, especially as I reached the final stages of this journey.

Edmond, State of Oklahoma, U.S.A. 2024

Part I

Introduction

Chapter 1

Introduction

In this project, the aim is to reconstruct images of various objects by utilizing the filtered back projection algorithm. The primary objective of this thesis is to investigate the application of microwave antennas across a range of frequencies to detect and identify changes in dielectric properties within a uniform background. The resulting 2D images will depict the shapes of the objects and contribute to advancements in imaging techniques, including applications in animal image reconstruction.

This thesis will provide a rationale for the chosen approach and discuss the fundamental concepts underpinning the methodology. It begins with an introduction to the historical context of the topic, followed by a chapter that outlines the theoretical framework applied in this study. The subsequent chapter details the experiments and simulations conducted to achieve the desired results. The findings are presented in the final chapter, along with a summary and conclusion.

1.1 Brief History

Over the past 150 years, significant advancements have been made in the application of electromagnetic waves since their existence was confirmed by Hertz, following James Clerk Maxwell's theoretical work. The field of medical imaging began in 1897 with Roentgen's discovery of X-rays, a revolutionary milestone. Soon after, Marie Curie was awarded the Nobel Prize for her groundbreaking research on radiation. Thomas Edison further advanced imaging by inventing the fluoroscope, which utilized fluorescent materials to achieve sufficient image intensity for commercial use. This innovation enabled the visualization of bones and tissues, a critical medical breakthrough that quickly gained international adoption. However, it wasn't until the 1940s that the long-term harmful effects of radiation exposure were acknowledged and documented [1]. Meanwhile, the Radon transform, a mathematical foundation for modern imaging techniques, remained theoretical due to the lack of necessary technological advancements.

Figure 1.1: Fluoroscope at Ottawa Hospital

Radar technology traces its roots to wireless communication. In 1897, Alexander Popov observed interference caused by a passing ship during wireless signal transmission. This observation laid the groundwork for radar principles. In 1904, German inventor Christian Hülsmeyer created the telemobiloscope, a 650 MHz continuous-wave device capable of detecting ships up to two miles away in dense fog. Despite its innovation, its performance was limited by the lack of advanced electronics and antenna systems. In 1914, Nikola Tesla, renowned renowned for his work in alternating current (AC) systems, proposed the concept of radar.

Later, in 1922, Guglielmo Marconi, a Nobel Prize laureate, delivered a lecture discussing radar principles. Around this time, radar research gained traction across various nations involved in wartime efforts, reflecting contributions from scientists worldwide [2].

The first radar system utilizing the Doppler principle was developed in 1935, designed to detect vehicles in the pre-World War II era [3]. By the end of World War II, radar technology had reached unprecedented levels and continued to evolve rapidly in the post-war period, driving advancements in electronics and paving the way for microwave technology. Radar applications in medicine did not emerge until the early 1970s. Early uses included measuring organ movements and detecting water condensation in the lungs, marking the beginning of radar's integration into medical diagnostics.

1.2 Medical Imaging

Over the past 20 years, microwave imaging (MWI) has gained attention as an alternative technique for imaging and diagnosing tumors [4]. In the field of nondestructive testing and evaluation, significant research has focused on developing electromagnetic (EM) imaging methods to detect and analyze hidden structures. These methods often rely on specific frequency bands, including the microwave band (300 MHz to 30 GHz), the millimeter-wave band (30 GHz to 300 GHz), and the terahertz band (300 GHz to 3 THz) [5]. This project focuses primarily on the microwave band, specifically between 1 GHz and 6 GHz, within the broader range of 300 MHz to 30 GHz. The reasons for selecting this frequency range will be explained in the next chapter, highlighting the properties that make it most suitable for imaging purposes.

An imaging system generally consists of two main components: hardware and signal processing (or imaging algorithms). The hardware includes the instrument setup, antennas, measurement devices, and recording tools, while the signal processing component interprets the "collected data" to determine the electrical and geometric characteristics of the object being studied. Both elements are crucial for achieving high-quality image reconstruction. Imaging techniques are generally categorized into two types: quantitative methods and qualitative methods [6].

Advances in modern computing have significantly improved the ability to solve complex mathematical problems, such as the inverse scattering problem, which has historically posed challenges. These issues are addressed by reformulating the problem into an optimization framework, though this approach introduces limitations related to validity and the potential for misrepresenting physical phenomena. Various approaches have been developed to detect, locate, and map different types of tissue, each employing distinct methodologies [7][8].

While microwave imaging offers the potential for improved resolution, it also presents several challenges. Biological tissues are heterogeneous, leading to complex field distributions within the body. Addressing these challenges requires efforts to minimize interference from artifacts surrounding the area of interest. For instance, when imaging the brain, the skull, skin, fat layers, and cerebral fluid can interfere, while breast imaging, factors such as the skin, nipple, and chest wall create similar issues. Additionally, embolisms and early-stage tumors are often only a few millimeters in size, demanding high-resolution imaging to detect them accurately. However, achieving high resolution comes with trade-offs, particularly between spatial resolution and depth penetration due to signal losses.

The need for high resolution significantly increases the computational demands for image reconstruction. Moreover, the anatomical differences between patients add another layer of complexity to the imaging process. Depending on the specific imaging scenario, unique challenges arise that require tailored approaches and system configurations to address the distinct physical characteristics of the area being examined [9].

1.3 Motivation and Purpose

Modern imaging systems are often characterized by their large size, high cost, and invasive nature, including exposure to radiation and the use of fluorescent contrast agents. While the medical field has developed reliable diagnostic tools, they are not without drawbacks, such as the risk of ionizing radiation, which is linked to cancer, as well as significant size and energy consumption. These limitations highlight the need for advancements in imaging technology. Affordable and dependable imaging systems could bring significant benefits to developing countries, enhancing global healthcare accessibility. Introducing cost-effective and reliable medical imaging solutions has the potential to improve public health worldwide. Rapid diagnostic capabilities are especially critical in emergency situations, such as strokes, where correctly identifying the type of stroke (e.g., internal bleeding or a thrombus) and initiating treatment within a few hours can save lives.

The objective of this thesis is to demonstrate the feasibility of high-resolution microwave imaging for detecting objects and biological tissues. Although commercial applications of microwave-based imaging are currently limited in the medical field, microwaves are already widely used in other areas such as ground-penetrating radar, wall imaging, and heartbeat monitoring. This study aims to replicate the concept by generating an ultra-wideband (UWB) signal, applying it to a simulated phantom, capturing the backscattered signals, and reconstructing an image using the Filtered Back Projection algorithm. The approach will then be validated through experiments on real mice to assess their practical applicability.

Chapter 2

Background

This section offers a comprehensive overview of the theories and formulas applied in this project. It includes an analysis of wave propagation physics, the basic principles and applications of antenna aperture theory, and the core concepts of signal processing.

2.1 Wave Equation

In physics, a wave is defined as a disturbance that carries energy through matter or space, typically involving oscillations or vibrations in a medium or a field. For instance, sound waves propagate by the collision of air molecules, transferring kinetic energy as pressure variations, which categorizes them as mechanical waves. Unlike mechanical waves, electromagnetic waves do not need a medium to travel; they consist of periodic oscillations in electric and magnetic fields, generated by charged particles. These waves differ in their wavelengths and are described by the wave equation, which outlines how the disturbance changes over time. Electromagnetic fields propagate in wave-like patterns, varying with both time and space.

Maxwell's equation in free space

Wave propagation is explained through the wave equation, which is tailored to the characteristics of the medium and the applicable boundary conditions. For instance, James Clerk Maxwell formulated a theory detailing how electromagnetic fields propagate in free space.

$$\nabla \times \vec{E} = -\frac{\partial(\mu\vec{H})}{\partial t} \qquad \nabla \cdot \left(\varepsilon\vec{E}\right) = 0 \qquad \text{Faraday's law} \quad (2.1.a)$$

$$\nabla \times \vec{H} = \frac{\partial(\varepsilon\vec{E})}{\partial t} \qquad \nabla \cdot \left(\mu\vec{H}\right) = 0 \qquad \text{Ampere's law} \quad (2.1.b)$$

Where: $\vec{E}$ is the electric field intensity,
$\vec{H}$ is the magnetic field intensity
ϵ is the electric permittivity
μ is the magnetic permeability
and ∇ represent the gradient vector operator [13] [7].

The wave equation derived from Maxwell's equation is $\nabla^2\vec{E} = \frac{1}{c^2}\frac{\delta^2\vec{E}}{\delta t^2}$ (2.1.c)

where c is the speed of propagation, and ∇^2 represents the Laplacian operator

A signal propagating in three-dimensional space can be described as s (x, y, z, t), where x, y, and z represent spatial coordinates describing the signal's amplitude and displacement, while t accounts for its evolution over time. The properties of such a signal are crucial for understanding its behavior, including the direction and speed of propagation, as well as its frequency components in both space and time. Temporal frequency, expressed as cycles per second (Hz), indicates the number of oscillations per unit of time, while spatial frequency, measured in cycles per meter, represents the number of oscillations per unit of distance.

Because the wave equation in free space is linear, more complex wave solutions can be constructed by summing or integrating simpler ones. Using Fourier Theory, any waveform can be represented as an integral of complex exponentials. Thus, the signal s (x, y, z, t) can be expressed in the form of a complex exponential to model its behavior and characteristics.

$$s\,(x, y, z, t) = A exp\,(j(\omega t - k_x x - k_y y - k_z z)) \qquad (2.1.d)$$

The vector (kx,ky,kz), known as the wave vector, represents the spatial wavenumber, similar to how ω corresponds to temporal frequency. In this context, the wave vector $k^{\rightarrow}$ characterizes spatial frequency. For the signal to comply with the wave equation, it must adhere to a specific constraint.

$$\vec{k}^2 = \frac{\omega^2}{c^2} \qquad (2.1.e)$$

The process of solving Maxwell's equations to calculate the electric field based on known sources, obstacles, and the dielectric properties of the object of interest is referred to as the forward scattering problem. Conversely, determining the dielectric properties of a medium using known values of the electric field and the source is known as the inverse scattering problem [6]. Solving the inverse scattering problem often requires assumptions about wave propagation, which can introduce errors if not carefully addressed. This remains a significant and unresolved challenge in the field of RF technology.

2.2 Attenuation

In practical scenarios, every medium through which a wave propagates exhibits some degree of loss. When attenuation is considered, the wave equation for the electric field is modified accordingly to account for this effect.

$$\nabla^2 E = \frac{1}{c^2} \cdot \frac{S^2 E}{\delta t^2} + (\varepsilon\mu + \sigma)\frac{\delta \vec{E}}{\delta t} \qquad (2.2.a)$$

In reality is that the dielectrics are not perfect which results in a slightly different effect. Free or bound carriers can result in both heating and losses. Dissipation can be characterized as an imaginary component with a relative permittivity [23]

In free space, the dielectric constants are frequency-independent, making the medium non-dispersive, with relative permittivity ϵ_r and relative permeability μ_r both equal to 1. This simplifies the wave equation to describe the speed of light [22]. However, in real-world materials, dielectrics are not ideal, leading to slightly different behavior. The presence of free or bound charge carriers can cause both heating and energy loss. This dissipation effect can be modeled as an imaginary component of the relative permittivity [23].

$$\varepsilon = \varepsilon^{(1)} + j\varepsilon^{(2)} \quad (2.2.b)$$

where $\varepsilon^{(2)}$ is called the dielectric absorption as it intervenes in the equation for the electrical energy. And is usually expressed in terms of loss tangent δ with the relation:

$$\tan\delta = \frac{\varepsilon^{(2)}}{\varepsilon^{(1)}} \quad (2.2.c)$$

Dielectrics

The definition of dielectrics (or dielectric materials) is the electromagnetic properties of a medium. The wave equation is a function of electric permittivity ε, magnetic permeability μ. In general, the velocity of propagation is:

$$c = \frac{1}{\sqrt{\mu_0 \mu_r \varepsilon_0 \varepsilon_r}}$$

Where: μ_0 = 1.261˙0−6 *Hm*−1, absolute magnetic permeability of free space

ε_0 = 8.861˙0−6 *Fm*−1, absolute electric permittivity

μ_r relative magnetic permeability of the medium

ε_r relative electric permittivity of the medium

In free space, these dielectric constants that are independent of frequency and the medium is not hence dispersive ($\varepsilon_r = 1$, $\mu_r = 1$) simplifies the equation to the velocity of light. In reality is that the dielectrics are not perfect which results in a slightly different effect. Free or bound carriers can result in both heating and losses. Dissipation can be characterized as an imaginary component with a relative permittivity [23]

In free space, the dielectric constants are frequency-independent, making the medium non-dispersive, with relative permittivity ϵ_r and relative permeability μ_r both equal to 1. This simplifies the wave equation to describe the speed of light [22]. However, in real-world materials, dielectrics are not ideal, leading to slightly different behavior. The presence of free or bound charge carriers can cause both heating and energy loss. This dissipation effect can be modeled as an imaginary component of the relative permittivity [23].

$$\varepsilon = \varepsilon^{(1)} + j\varepsilon^{(2)} \quad (2.2.b)$$

where $\varepsilon^{(2)}$ is called the dielectric absorption as it intervenes in the equation for the electrical energy. And is usually expressed in terms of loss tangent δ with the relation:

$$\tan\delta = \frac{\varepsilon^{(2)}}{\varepsilon^{(1)}} \quad (2.2.c)$$

2.3 Radar Principles

Electromagnetic scattering occurs when an electromagnetic wave encounters a discontinuity or an object, causing the wave's trajectory to deviate. This change in the wave's direction is referred to as scattering. The way radar signals scatter or reflect depends on the wavelength of the electromagnetic wave and the shape of the object.

When the wavelength is much smaller than the size of the scatterer, the scattering primarily occurs in the forward direction, often referred to as optical scattering. If the wavelength is comparable to the size of the scatterer (within a few wavelengths), resonances may develop, leading to variations in scattering intensity across different frequencies. This phenomenon is known as Mie scattering or resonant scattering, with most scattering occurring in the forward direction and some in the backward direction.

When the wavelength is significantly longer than the size of the scatterer, the wave disperses around the object, resulting in scattering in all directions. This is known as Rayleigh scattering [22]. These different scattering behaviors are typically illustrated relative to a sphere, as shown in Figure 2.3.1 on the next page.

The scattering cross-section σ of a sphere with radius aa can be represented as a function of its circumference. For large spheres, the asymptotic behavior is described by the following expression:

$$\sigma_{sphere} = \pi a^2, \qquad \lambda << a \qquad (2.3.a)$$

For small spheres (Rayleigh region) the asymptotic expression is

$$\sigma_{sphere} = \pi a^2 9(ka)^4, \qquad a << \lambda \qquad (2.3.b)$$

(k is the wave number) which is defined as: $k = \frac{2\pi}{\lambda}$

It's important to highlight that the cross-section of a cylinder is

$$\sigma_{cylinder} = \frac{2a\pi L^2}{\lambda} \qquad (2.3.c)$$

2.3.1 Reflection and Transmission

Reflection and transmission of light are often simplified as the change in direction of an incoming ray and the opacity of an object. While this is accurate to some extent, the underlying cause of these phenomena lies in changes in wave propagation speed. When an incident wave encounters discontinuity between two media with different properties, a reflected wave and a transmitted wave are produced due to the abrupt change in propagation speed.

The difference in permittivity between the two media causes the wave velocity to vary, leading to a buildup of photons at the boundary as the light transitions into the new medium. This results in some photons "bouncing off" the surface, creating the reflected wave, while others pass through, forming the transmitted wave. The reflected wave follows the law of reflection, where the angle of reflection equals the angle of incidence, while the transmitted wave undergoes refraction, governed by Snell's Law.

This principle is the foundation for using electromagnetic fields to detect distant or concealed objects. By analyzing the reflected and transmitted waves, which experience specific losses and directional changes, information about the second medium can be inferred if the properties of the first medium are known. However, this explanation is simplified, as real-world scenarios involve multiple factors affecting wave loss and direction when interacting with complex structures. Nevertheless, it outlines the core concept behind radio detection and ranging (RADAR).

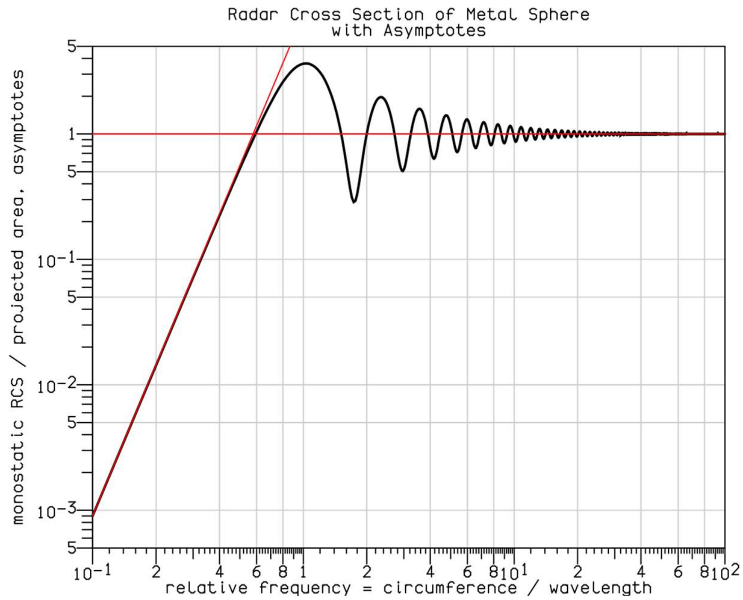

Figure 2.3.1: Radar cross section vs relative frequency [15]

2.3.2 Electromagnetism in Biological Tissue

There are ongoing safety concerns regarding the potential biological effects of electromagnetic radiation. Over time, the field has become more advanced, leading to the development of safety guidelines and methods for accurate measurement.

Although radio frequency (RF) radiation is classified as non-ionizing, it still transfers energy, which can be absorbed by the human body. Without proper precautions, this energy absorption could lead to harmful effects. Since people are continuously exposed to microwave sources in everyday life, public safety standards have been established to mitigate risks.

One key measure used to assess the impact of RF exposure is the Specific Absorption Rate (SAR). SAR quantifies the rate at which energy from an electromagnetic field is absorbed by human tissue, expressed as power absorbed per unit mass of tissue. It is calculated using the following equation:

$$SAR = \frac{1}{v}\int \frac{\sigma(r)|E(r)|^2}{\rho(r)}$$

Where: σ is the sample electric conductivity

E is the root mean squared (RMS) electric field

ϱ is the sample density

V is the volume of the sample.

The Specific Absorption Rate (SAR), measured in watts per kilogram, can be correlated with temperature changes in human tissue. Various organizations have developed standards to ensure public safety through extensive testing and research [13]. In the United States, these standards are established by the Federal Communications Commission (FCC), while in Europe, the European Telecommunications Standards Institute (ETSI) defines its own guidelines.

Currently, there are no specific standards for Ultra-Wideband (UWB) radar scanners, as these devices have yet to be fully realized. However, regulations for generic UWB applications are in place to provide a framework for their use [14].

2.4 Image Reconstruction Method

The Filtered Back Projection (FBP) algorithm is a key method used in modern medical imaging to reconstruct images from collected data. It is a quick and straightforward approach to creating medical images. As the name implies, FBP involves two primary steps: first, filtering the data along the detector's rows, and second, using back projection to map the filtered data back into the image, following the paths along which the data was originally captured.

2.4.1 Forward Projection in Image Reconstruction

Forward projection in image reconstruction involves simulating how data is collected by projecting an image onto a detector. To explain this concept, we can use a simple 3×3 image matrix where each pixel has a specific intensity value, similar to a CT image but on a much smaller scale (real CT images typically have 512×512 pixels or more).

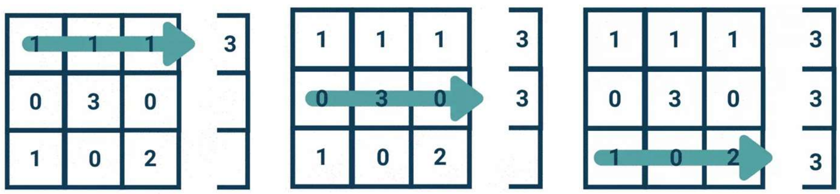

Fig 2.4.1.a: Example of parallel beam projection from the left to the right [16]

The forward projection process is an additive operation: it sums up the pixel values along specific paths, known as rays, as they pass through the image. For example, in parallel beam projections, rays move from one side of the image to the other (e.g., left to right), adding up the values of the pixels they pass through. This process generates projection data that represents the sum of intensities along each ray.

If only one view of projection data is available, it won't be enough to reconstruct the full image, as all detector values could be identical, providing limited information. To fully reconstruct an image, projection data from 180 degrees is typically required. For instance, when the forward projection is rotated 90 degrees from the initial direction, it reveals new information. In the first case, all detector values might be identical, but in the rotated projection, each detector has distinct values. These unique measurements from various angles combine to produce a complete CT image.

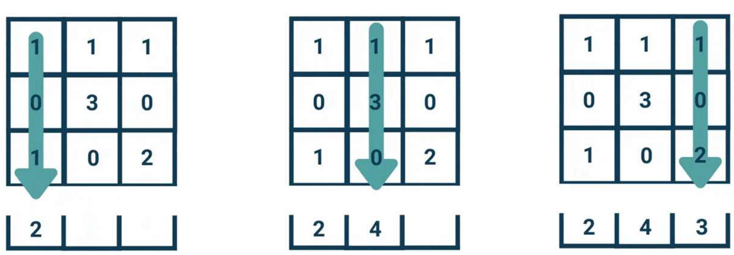

Fig 2.4.1.b: Example of parallel beam projection from the top to the bottom [16]

2.4.2 Back Projection in Image Reconstruction

Back projection in image reconstruction is a process that essentially reverses the forward projection. While forward projection transfers data from the image domain to the detector domain, back projection maps the detector data back onto the image domain.

For example, imagine a simple 3×3 matrix. During back projection, the values from the detector are redistributed into the image matrix, following the same paths or directions used during the measurements. This operation helps reconstruct the original image from the collected projection data.

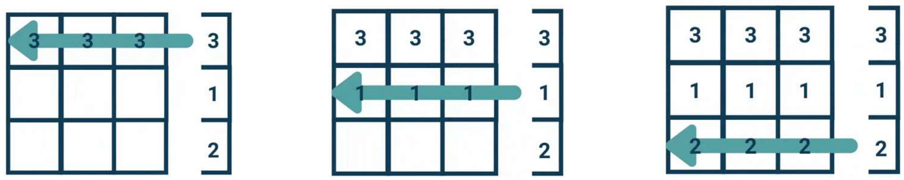

Fig 2.4.2: Example of parallel beam back projection from the right to the left [16]

2.5 Ultra-wide Band

Ultra-Wideband (UWB) wireless technologies distribute signals across a broad spectrum and have a wide range of applications, including military, security, civilian, commercial, and medical fields. UWB offers several advantages, particularly in environments prone to multipath propagation issues. Its broad bandwidth improves resistance to reflections and propagation challenges.

Additionally, UWB can transmit multiple signals simultaneously, which increases data rates. Its low power levels reduce interference with other signals in the same spectrum, making it appear more like background noise than a disruptive signal. UWB is also more secure due to its low probability of interception and the difficulty of recovering its signal.

UWB signals are characterized by a fractional bandwidth of 20-25% of their center frequency or by occupying at least 0.5 GHz of the spectrum, as defined by international regulatory bodies such as the FCC and ITEAS. The fractional bandwidth (B_f) is calculated using the following definition:

$$B_f = 2\frac{f_h - f_l}{f_h + f_l} \tag{2.5.a}$$

Where: B_f = Fractional Bandwidth in Hz

f_h = the highest -10dB frequency point of the signal spectrum

f_l = The lowest -10dB frequency point of the signal spectrum [24]

A suggested approach for improving resolution in wide-band data processing involves estimating the signal subspace across multiple frequency channels. This is achieved by dividing the bandwidth into several narrow bands and combining the information from these different frequency ranges. The goal is to minimize sidelobes by aligning the transformed steering matrices at various frequencies to be as similar as possible. However, this method has a drawback: it increases the noise floor relative to the main lobe [11].

Resolution

Range resolution refers to the capability to differentiate objects based on their distance along the same axis or depth relative to the transmitter/receiver. This is akin to depth perception. The range resolution is determined by the pulse duration, denoted as τ.

$$s_r = \frac{C \cdot \dot{\tau}}{2} \tag{2.5.b}$$

Where: c is the speed of light

S_r is the angular resolution (the division by 2 terms of the reflected signal propagation distance)

The relationship between the bandwidth B and a pulse duration τ is

$$B = \frac{1}{\tau} \tag{2.5.c}$$

A wide bandwidth leads to a short pulse duration, giving Ultra-Wideband (UWB) technology its excellent time resolution. This makes it highly suitable for precise ranging applications. Unlike angular and cross-range resolution, which depend on wavelength, UWB's fine time resolution is independent of wavelength.

UWB signals can penetrate various materials, including the human body, and are non-ionizing, making them ideal for a wide range of non-invasive applications. Different tissues and body masses have unique reflection indices, allowing the use of UWB's narrow time signals to differentiate between tissue types. This capability is particularly valuable for applications such as health monitoring, patient examinations, and the detection and imaging of tumors [24].

2.6 S-parameters

The ability to simplify most passive and active devices, regardless of their circuit complexity or nonlinear behavior, into a straightforward input-output relationship offers significant advantages. The "black box" approach is particularly valuable in RF and microwave circuit design, where solving Maxwell's equations fully can be either too complex or unnecessary for practical purposes, such as designing systems like filters and resonators.

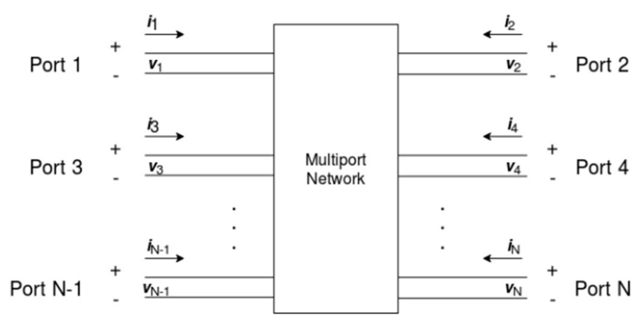

Figure 2.6.a: General multi-port network [20]

$$a_n = \frac{1}{2\sqrt{z_0}}(V_n + z_0 I_n) \quad (2.6.a)$$

$$b_n = \frac{1}{2\sqrt{z_0}}(V_n - z_0 I_n) \quad (2.6.b)$$

Where: Z_0 is input impedance,
V_n Voltage at port n,
I_n Current at port n.

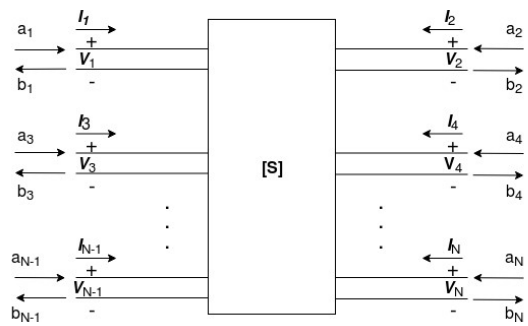

Figure 2.6.b: General S-port network [20]

When the input and output impedances are equal, the voltage and current can be expressed using the following relationships:

$$I_n = \frac{1}{\sqrt{z_0}}(a_n + b_n) \quad (2.6.c)$$

$$V_n = \sqrt{z_0}(a_n + b_n) \quad (2.6.d)$$

Separating the forward and backward traveling wave components gives rise to the following expression:

$$a_n = \frac{V_n^+}{\sqrt{z_0}} = \sqrt{z_0} I_n^+ \quad (2.6.e)$$

$$b_n = \frac{V_n^-}{\sqrt{z_0}} = -\sqrt{z_0} I_n^- \quad (2.6.f)$$

2.6.1 Vector Network Analyzer

The Vector Network Analyzer (VNA) is a widely used RF test instrument, particularly valuable for RF design applications. It evaluates the performance of radio frequency and microwave devices by measuring their complex S-parameters, capturing both the amplitude and phase of single- or multi-port networks. This data is critical for designers, offering insights into components and circuits that are unattainable with other types of test equipment.

The VNA operates by measuring voltage in terms of magnitude and phase. It performs a frequency sweep over a specified range, analyzing the transmitted and reflected responses relative to the incident signal at each frequency. This enables the calculation of S_{nm} parameters. Since both amplitude and phase are measured, the data provides a wealth of information, allowing time-domain characterization to be derived from the frequency response [30].

Figure 2.6.1: 6GHz 3-port Vector Network Analyzer [20]

2.6.2 Frequency and Time Domain

The frequency domain represents signals or functions in terms of frequency rather than time, commonly used in electronics, control systems, and statistics. Its graph shows the distribution of signal energy across different frequency bands. While time-domain graphs display how signals change over time, the two domains are interconnected and can be converted using mathematical transforms. For example, the Fourier transform breaks a time-domain signal into its sinewave frequency components, providing a frequency-domain representation. This process is reversible, allowing conversion back to the time domain [19].

$$F(\omega) = \int_{-\infty}^{+\infty} f(t) e^{-2\pi\omega} \, dt \qquad (2.6.2)$$

Studying physical sources requires working in the time domain, where phenomena are real, measurable, and time dependent. However, interactions of RF/MW fields with biological tissues are typically analyzed in the frequency domain, assuming sinusoidal sources, as many are nearly monochromatic [19].

2.7 Microwave Imaging

Microwave imaging is divided into radar imaging and microwave tomography (MWT). MWT involves solving a nonlinear inverse scattering problem to map the dielectric properties of a target, whereas radar imaging solves a simpler linear inverse problem to locate contrasts in the imaging medium but cannot determine dielectric values.

Radar methods analyze object reflections to detect targets. Synthetic Aperture Radar (SAR) improves resolution by simulating a larger aperture with a moving single-element transmitter. SAR focuses on phase shift measurements, disregarding amplitude, as amplitude attenuation depends on factors like radar cross-section, antenna-target distance, and electromagnetic losses.

Microwave Tomography

Current clinical imaging methods include computed tomography (CT), positron emission tomography (PET), and magnetic resonance imaging (MRI). These techniques provide valuable insights into tissue properties like ischemia, infarction, hypoxia, metabolism, and malignancies, each with strengths and limitations. CT offers high spatial resolution but is less effective for soft-tissue imaging compared to PET [7].

Microwave tomography is a noninvasive, wave-based imaging method that uses electromagnetic radiation instead of light to view inside objects. It creates images of dielectric properties, such as permittivity and permeability, based on measured electric fields. The relationship between these properties and the measured fields is nonlinear and modeled using Maxwell's equations [6].

Part II

The project

Chapter 3

Implementation and Method of approach

The approach taken in this project involves reconstructing images from both simulated data and experimental measurements of various objects in the lab, selected for their dielectric properties resembling human tissue. Additionally, measurements performed on live mice, as part of ongoing research under the advisor's supervision, will also be discussed.

Simulations play a critical role in testing the Filtered Back Projection algorithm, assessing resolution improvements with varying parameters, and evaluating the effects of noise. These steps provide valuable insights before applying the method to different phantoms, ultimately guiding the design of an imaging device.

Figure 3.1: Illustration of approach

Figure 3.1 above outlines the methodology used for developing data collection and reconstructing images, with each stage addressing specific aspects. Both the simulation and trial stages emphasize preparation for image reconstruction.

The data collection process takes place in a chamber lined with RF absorbers to eliminate unwanted noise from the environment and the system's automated base.

3.1 Hardware and Software Tools

The resources and tools utilized during this project are outlined in the subsections below:

3.1.1 Arduino and Continuous Servo Motor

Using an Arduino microcontroller to build an automated base for microwave imaging data collection not only simplifies the process but also enhances data accuracy and image quality. By integrating precise motor control and customizable programming, this system can significantly improve imaging experiments.

A continuous servo motor, controlled by the Arduino, ensures precise and consistent rotation of the base. This accuracy is crucial for collecting data at the specified angles and maintaining uniformity across measurements. With more angular increments (e.g., 5 degrees instead of 10), the system collects more data points, which helps improve the resolution and accuracy of the reconstructed image by providing finer details during the back projection process.

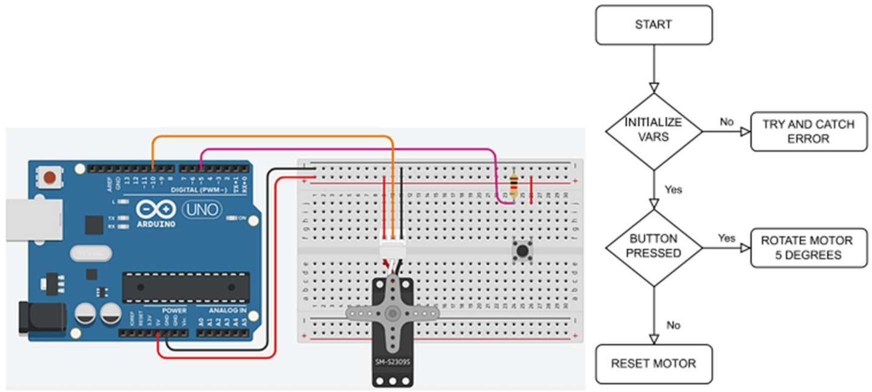

Figure 3.1.1: Schematic and flowchart of Auto Rotary Controller

3.1.2 RF Absorber

The RF absorber PU-RAM-P1000 is a specialized material used in image reconstruction experiments to minimize unwanted reflections and electromagnetic interference. It is designed to absorb radio frequency (RF) waves across a wide frequency range, ensuring a controlled environment for accurate data collection. By reducing stray signals and environmental noise, the PU-RAM-P1000 enhances the reliability and precision of imaging systems, such as those used in microwave tomography or radar-based imaging. Its use is critical in creating a noise-free setting, enabling more accurate reconstruction of images from the collected data.

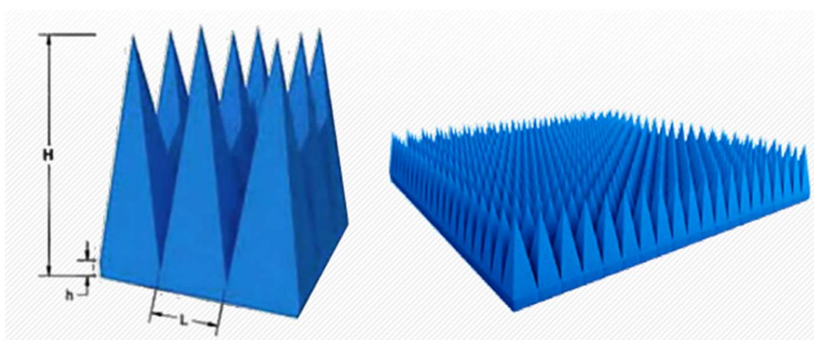

Figure 3.1.2: RF absorber PU-RAM-P1000 [18]

3.1.3 Log Antenna

The Ultra-Wideband (UWB) 1.35GHz-9.5GHz Log-Periodic Directional RF Antenna is a critical component in image reconstruction systems, particularly for microwave imaging applications. This antenna is designed to operate across a wide frequency range, enabling it to capture and transmit detailed electromagnetic signals. Its directional properties provide focused radiation patterns, improving signal clarity and reducing interference from surrounding noise. The broad bandwidth of the antenna is ideal for capturing high-resolution data, as it supports diverse frequency components necessary for accurate image reconstruction. Its versatility and precision make it a valuable tool in applications such as medical imaging, non-destructive testing, and radar-based imaging systems.

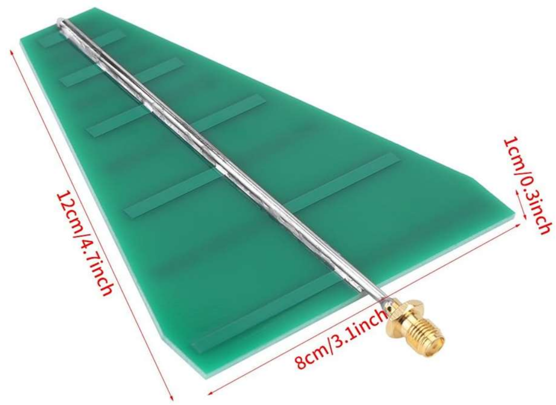

Figure 3.1.3: Ultra-Wide Band 1.35GHz-9.5GHz Log-Periodic Directional RF Antenna [19]

3.1.4 VNA -0460e

Scattering parameters from a 3-port network produce nine outputs, where Snn represents the reflected signal relative to the incident signal, and Snm or Smn represent transmitted signals. Unlike time-domain signals, a VNA sweeps frequencies across a chosen range and step size, making the modulation less intuitive. Applying an inverse Fourier transform to the S-parameters reveals a Gaussian wavelet with a single zero-crossing point, which is ideal. Adjusting the frequency range changes the wavelet's pulse width, helping to accurately locate its center. This precision is crucial for estimating object range by analyzing reflected waves and signal delay. A frequency sweep from 0.4 GHz to 4 GHz corresponds to a total transient time of approximately

$$time = \frac{N_{sample}}{BW} \tag{3.1.4}$$

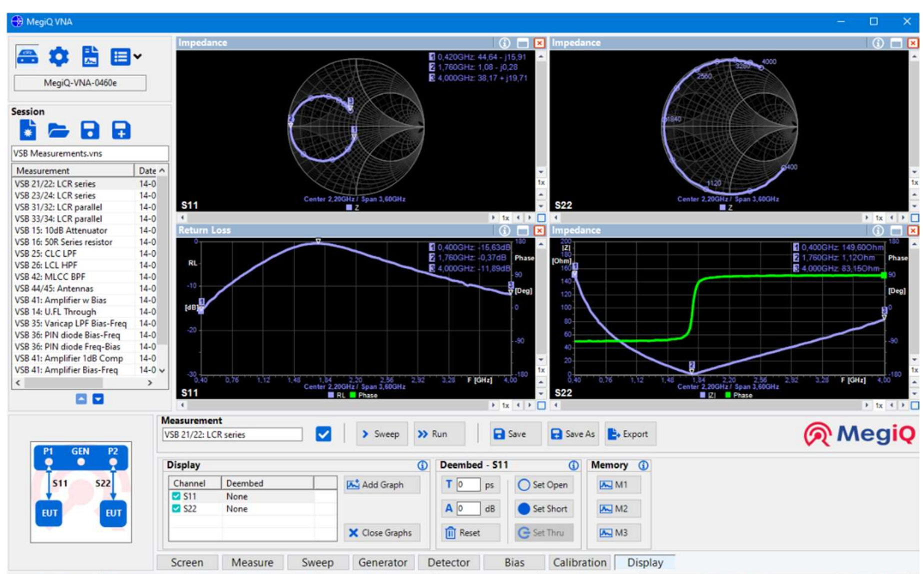

Figure 3.1.4: VNA integrated software [20]

3.1.5 Others

MATLAB: MATLAB is a powerful tool for image reconstruction, offering a wide range of built-in functions and toolboxes for processing and analyzing data. It enables the implementation of algorithms such as filtered back projection, Fourier transforms, and iterative reconstruction methods. MATLAB's ability to handle large datasets, visualize results, and perform numerical computations makes it ideal for reconstructing images from raw data in applications like medical imaging, tomography, and microwave imaging. Its flexibility allows researchers to customize algorithms and refine reconstruction techniques efficiently.

Anesthetic System: An anesthetic system for mice ensures humane and precise delivery of anesthetic agents, such as isoflurane, during experiments. It includes features like controlled gas regulation, oxygen supply, waste gas scavenging, and temperature maintenance to prevent hypothermia. Vital signs such as heart rate and respiration are monitored to ensure stability, and heated surfaces help maintain body temperature. These systems are essential for ethical and reliable research in fields like pharmacology, surgery, and imaging, minimizing stress and ensuring the welfare of animal subjects.

3.2 Choice of Inputs

Range resolution depends solely on pulse duration, as explained earlier, and is inversely related to signal bandwidth. Therefore, it is essential to simulate a time pulse based on these principles.

3.2.1 Pulse Modulation

The Gaussian function, which represents the probability density of a normal distribution, can be adapted to function as a time-dependent equation.

$$G(t) = \frac{1}{\sigma\sqrt{2\pi}} e^{-\frac{(t-t_0)^2}{2\sigma^2}} \quad (3.2.1.a)$$

The scaling factor is disregarded, utilizing only the exponential function to envelope a sine wave. The resulting equation used for the excited pulse s(t) is:

$$s(t) = V_{amp} * e^{-\{t-t_0\}^2/(2\tau^2)} \cos(2\pi f_c (t - t_{off})) \quad (3.2.1.b)$$

where: *Vamp* is the amplitude of 1

t_0 is pulse center in time

τ which determines the temporal width of the pulse

f_c being the center frequency of 3.2 GHz

The excitation pulse consists of a sine wave enveloped by a Gaussian function, lasting 2 ns, with a time delay t_0 of 1 ns.

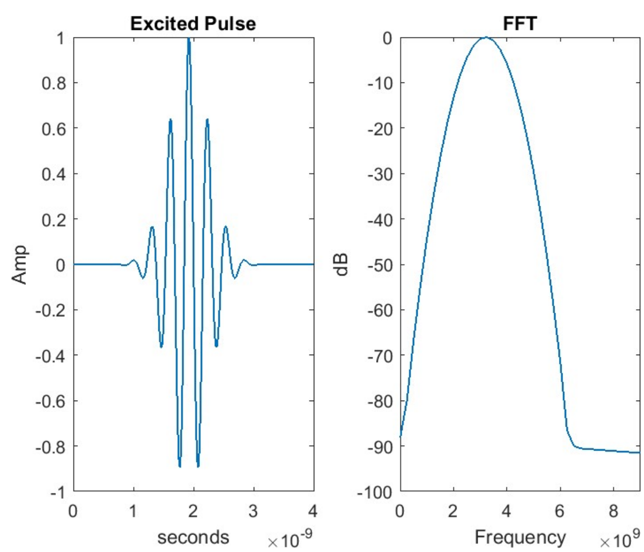

Figure 3.2.1: Excited pulse and its frequency response

Simulating a UWB radar signal requires careful selection of the impulse response. A shorter impulse duration corresponds to a wider bandwidth in the frequency domain. The input pulse should be a sine wave enveloped by a Gaussian function, with a total temporal width of 2 ns.

Figure 3.2.1 from the previous page illustrates the excited pulse generated by each transmitter. Analyzing the frequency response reveals a bandwidth ranging from 2 GHz to 5 GHz, meeting the UWB classification standards defined by FCC and ITEAS regulations.

3.2.2 Truncating Window Function

Truncating the frequency response reduces unwanted frequencies while preserving the center frequency as much as possible. However, this can lead to issues like higher sidelobes in the transformed domain, depending on the chosen window. A Fourier transform of a bell-shaped curve typically produces a sinc function. Figure 3.3 compares three window types based on main lobe width and sidelobe suppression. While the frequency response of a window appears in the time domain, this is explained by the Fourier transform's convolution properties. Truncating the frequency spectrum results in a sinc function in the time domain.

For simulating a UWB signal while minimizing unwanted frequencies, I selected the Hamming window with a 3.5 GHz center frequency. This window offers low sidelobe levels compared to the main lobe and falls within the antenna's operating range. Although attenuation is a drawback due to frequency-dependent loss, the Hamming window's narrow main lobe and low sidelobes make it ideal for this application.

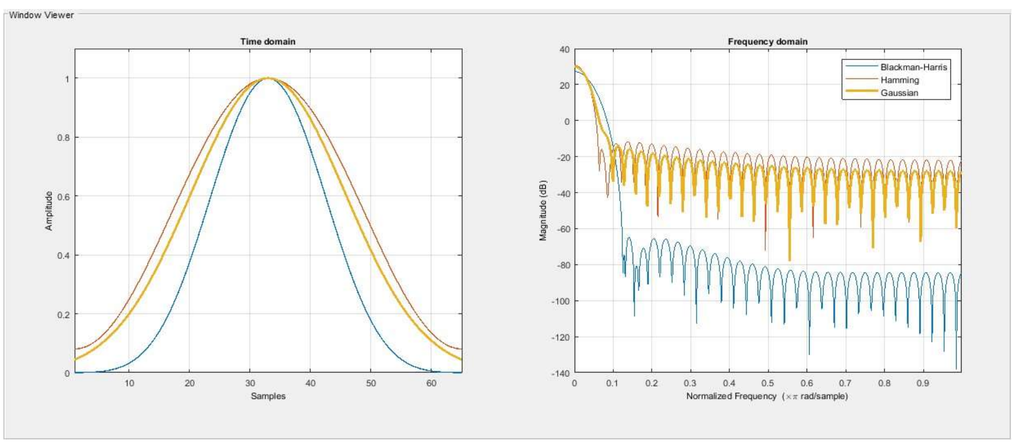

Figure 3.3: Comparing 3 window functions and their frequency transformation

The VNA signal response is trimmed around a central frequency of 3.5 GHz to focus on the target frequency range.

3.3 Phantom Design and Animal Experiment Setup

The goal is to create phantoms with dielectric properties similar to those of human brain tissue and fatty tissue. This will serve as a foundation for advancing microwave imaging techniques for detecting brain tumors and breast cancer in the future.

3.3.1 Design Properties of a Phantom

Various methods exist for creating dielectric phantoms, each varying in complexity and ingredient composition based on the requirements of the controlled test environment. The approach followed in this project involves using premade gel from Humimic Medical combined with readily available lab objects.

Figure 3.3.1.a: Example of premade gel from Humimic Medical [21]

This method is practical, environmentally friendly, and cost-effective, offering immediate applicability. The premade gels possess dielectric properties similar to various human tissues, ensuring consistent and reproducible phantoms while saving time and maintaining quality. Incorporating lab objects minimizes costs, promotes sustainability, and allows for flexible, customized setups. This combined approach enables scalable simulations of objects with diverse dielectric properties in a controlled environment.

(a) (b) (c)

Figure 3.3.1.b: (a) mix of gel 2 and gel 5

(b) center positioned square PLA and gel 5

(c) rock and gel 2

3.3.2 Animal Experiment Setup

This phase of the project is the primary focus of the study, as it involves utilizing a microwave imaging system to collect data and reconstruct microwave images of live animals—in this case, mice. The animal study was conducted at OUHSC as part of an ongoing research grant. All animal handling was performed by a trained individual from the pharmacy department, adhering strictly to established protocols and guidelines.

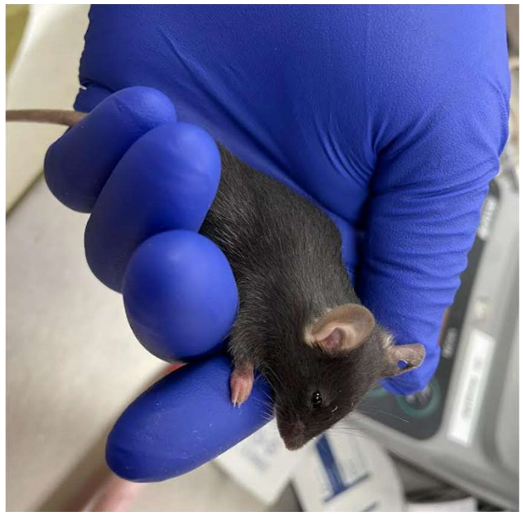

Figure 3.3.2.a: One of the mice used in animal study

We began the experiment with four mice at The University of Oklahoma Health Sciences Center. The lab personnel provided and administered an anesthesia system to ensure the mice were safely sedated throughout the process. Each mouse was placed inside a strainer while the anesthesia system remained active to maintain sedation. The strainer was then positioned within an automatic rotary microwave system, which collected microwave data for each mouse.

(a) (b) (c)

Figure 3.3.2.b: (a) mouse inside the anesthesia box
(b) mouse inside the strainer
(c) strainer placed inside the RF absorber chamber, along with a data collection system.

3.4 Image Reconstruction Process

Signal processing techniques play a crucial role in the overall process. Several steps are performed before achieving the final image reconstruction, many of which may not be immediately intuitive without further explanation.

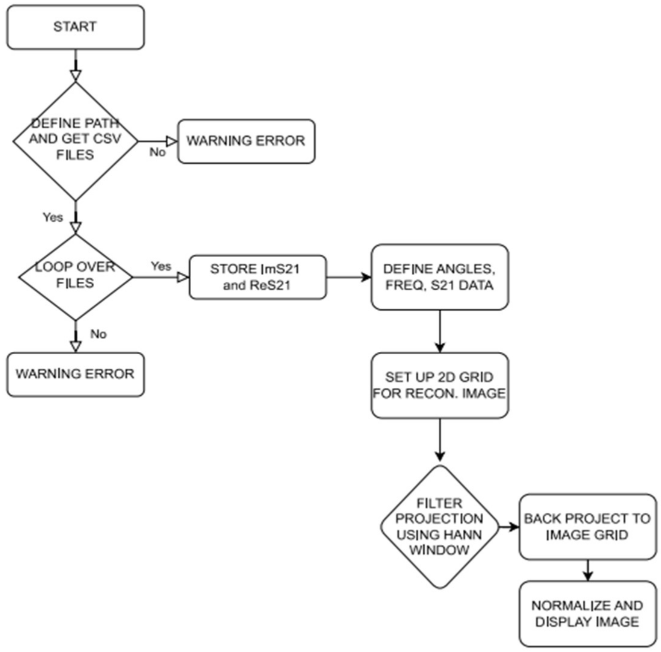

Figure 3.4.a: Flowchart for Object Image Reconstruction Process

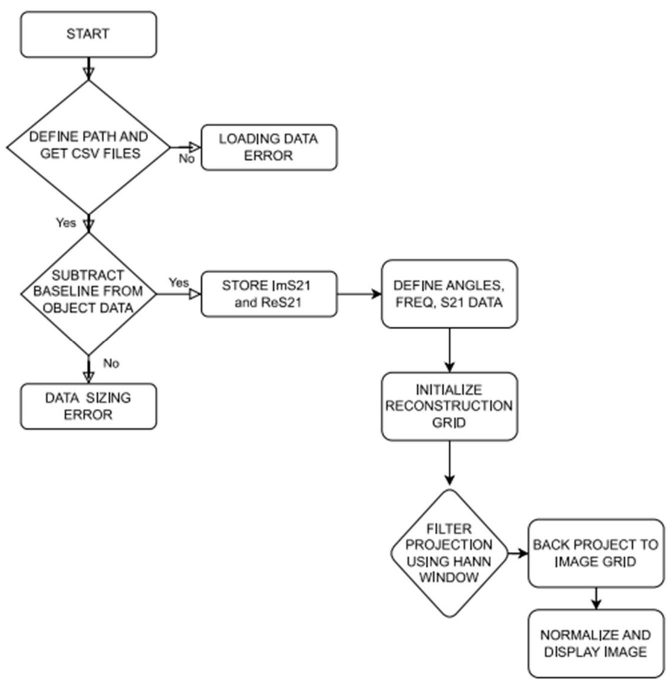

Figure 3.4.b: Flowchart for Mice Image Reconstruction Process

The main concept of artifact removal techniques in the live animal case is to isolate the scattered data caused by the object by subtracting the background's scattered data from the data collected when the object is present. In practical scenarios, artifacts such as skin tissue, bone, fat, and muscle tissue vary in thickness depending on the body location. Additionally, other artifacts unrelated to the body being imaged, like antenna coupling and direct propagation between nearby antennas, can occur. The preprocessing method should be tailored based on the type of artifacts present, which often require prior assumptions.

$$\mathbf{S}_{obj}(t) = \mathbf{S}(t) - \mathbf{S}_0(t) \tag{3.4.a}$$

where $\mathbf{S}_0$ is backscattered signals with no object present
$\mathbf{S}$ is backscattered signals with object present
$\mathbf{S}_{obj}$ is backscattered signals from the object o nly.

The choice of performing artifact removal in the time domain or the frequency domain depends on the specific technique employed. In the approach we followed, where measurements are taken both in the absence and presence of an object to subtract one from the other, the domain selection is straightforward and can be effectively demonstrated using the Fourier equation.

$$F[S(t) - S_0(t)] = \sum (S(t) - S_0(t)) e^{-j\omega t} \delta t = \sum S(t) e^{-j\omega t} \delta t - \sum S_0(t) e^{-j\omega t} \delta t \tag{3.4.b}$$

Chapter 4

Results

The key stages, decisions, and techniques involved in reconstructing an image of an object or a live animal from scattered data are outlined in this chapter. It presents results obtained through various approaches, emphasizing how different choices impact the quality of image reconstruction. The chapter includes insights into the latest imaging system, simulated data reconstructions, and the outcomes of image reconstruction efforts.

4.1 Imaging System

The latest imaging system setup used in the lab is illustrated in Figures 4.1.a and 4.1.b, showing configurations for object and mice image reconstruction. The VNA ports are connected to vertical antennas, while the auto-rotary base is configured to rotate clockwise. A laptop, along with a push-button controller, manages the rotation step, speed, and records each angle. The VNA is also connected to the laptop via dedicated software for data collection.

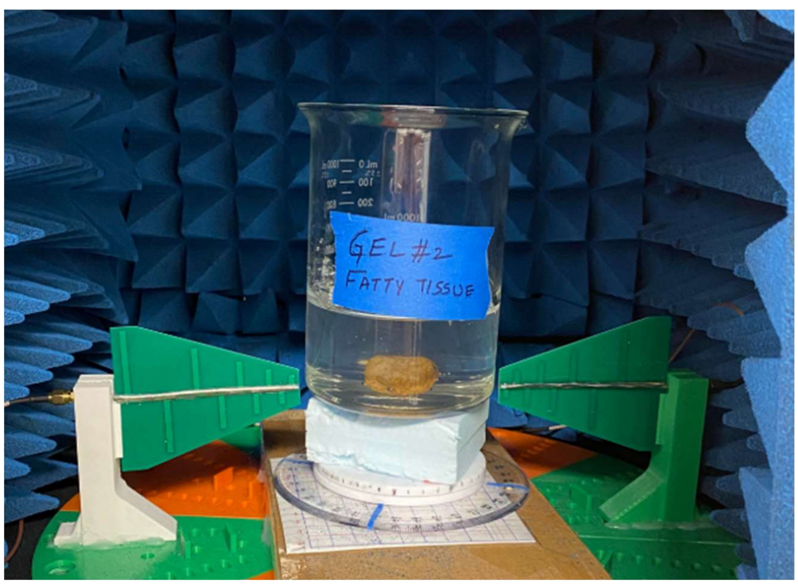

Figure 4.1.a: Latest setup for object image reconstruction

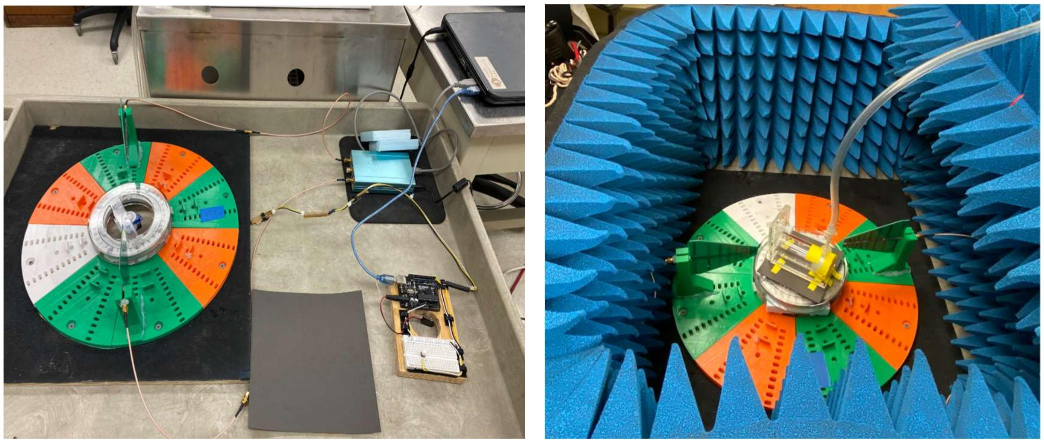

Figure 4.1.b: Final setup for mice image reconstruction

4.2 Reconstructed Image

4.2.1 Filter Back Projection Algorithm

We successfully tested the Filtered Back Projection (FBP) algorithm, achieving accurate image reconstruction from the collected projection data. The implementation demonstrated the algorithm's ability to handle the data effectively, producing clear and reliable results. This success marks a significant milestone in validating the approach and confirms the potential of FBP for practical applications in image reconstruction.

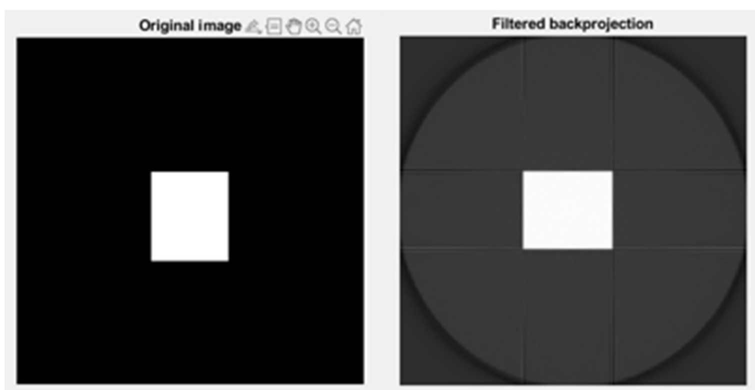

Figure 4.2.1: Original image on the left and reconstructed image on the right [16]

4.2.2 Object Reconstructed Image

The simulated phantom with various objects demonstrates the ability to detect objects in homogeneous environments. In this experiment Different gels were used such as Gel 2 simulates fatty tissue and Gel 5 simulates brain tissue. Figure 4.2.2(a) displays a 2D slice of Gel 2 and Gel 5, highlighting air pockets around them. Figure 4.2.2(b) shows an image of a square block, providing details about its density. Lastly, Figure 4.2.2(c) illustrates the shape of a stone, along with the air pockets surrounding it. In Figures 4.2.2(a) and (b), the images have been normalized to ensure all objects are displayed within a 1x1 scale. This normalization helps compare objects with varying densities more effectively.

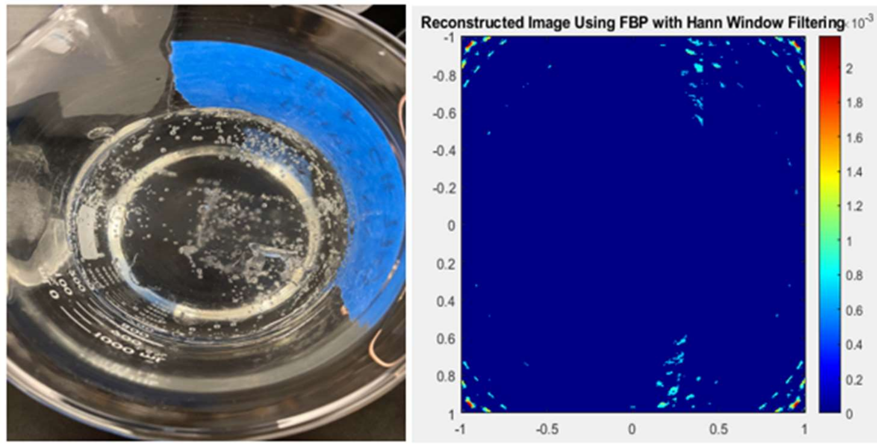

(a)

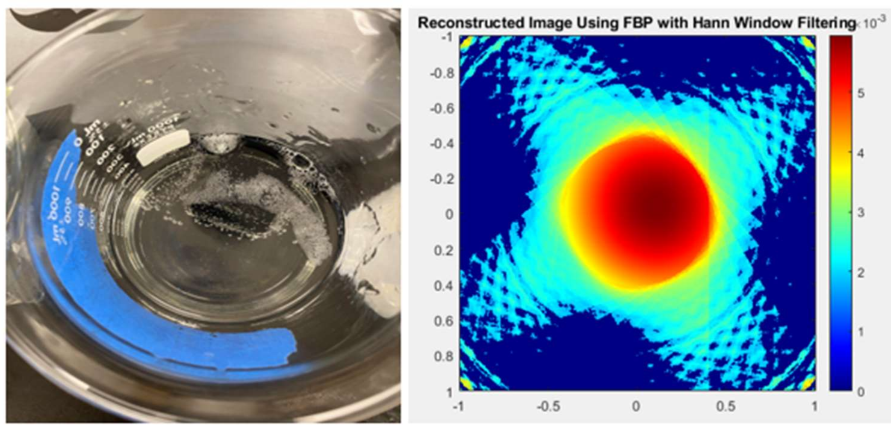

(b)

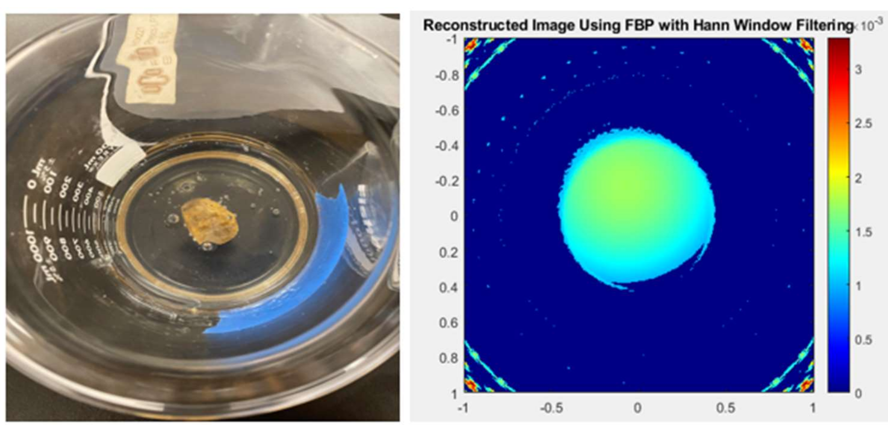

(c)

Figure 4.2.2 Phantom and its reconstructed image

(a) gel 2 and gel 5,

(b) gel 5 and square block,

(c) gel 2 and rock

The graphs for each phantom were compared to evaluate whether the objects could be distinguished based on their graph characteristics. For instance, with Gel 5 (represent brain tissue) and the square block (It is 100% filled with PLA material), a noticeable deep dip at 0.6 GHz suggests that the block's dielectric properties exhibit a strong response at this resonance frequency.

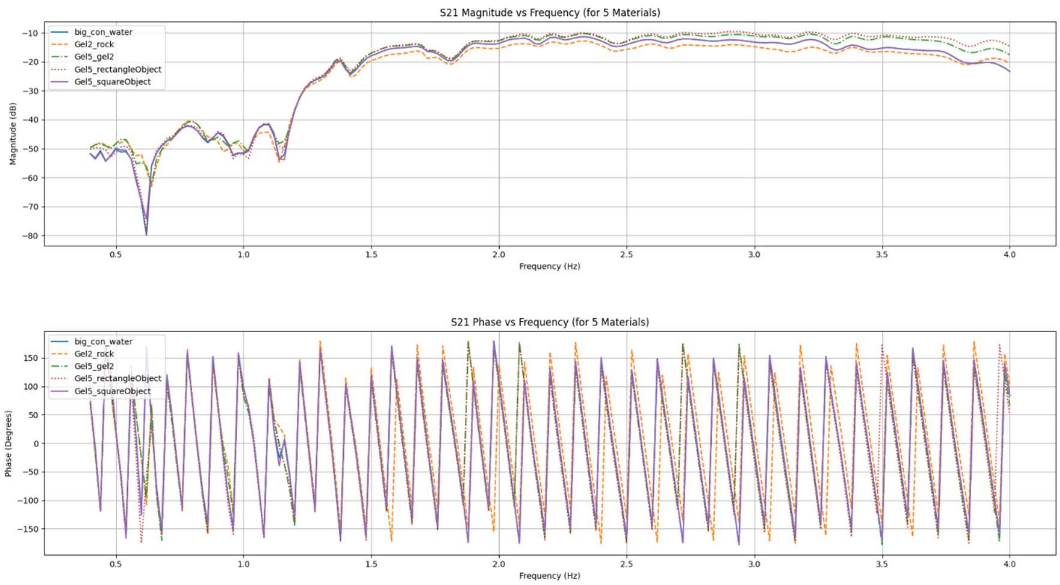

Figure 4.2.2.b: Dielectrics of gray tissue

Container	Mimicking	Relative Permittivity	Ingredients
Container 1	Fatty tissue and brain tissue	19.13	Gel 2 and gel 5
Container 2	Brain tissue with known object (square PLA block)	0.9999997	Gel 5 and square PLA block
Container 3	Fatty tissue and known object (rock)	4.784	Gel 2 and random rock

Table 4.2.2: Ingredients for each container and relative permittivity at 0.6 GHz

4.2.3 Animal Reconstructed Image

The reconstructed microwave images were compared to corresponding CT scans to evaluate their ability to detect and localize anatomical features. In both cases (male and female mice), the microwave reconstructions show a central pattern corresponding to the main bone structure and surrounding features, consistent with the CT images. The major anatomical structures, such as the organs and thoracic vertebrae, are identifiable in both imaging modalities, with the CT images serving as a high-resolution reference.

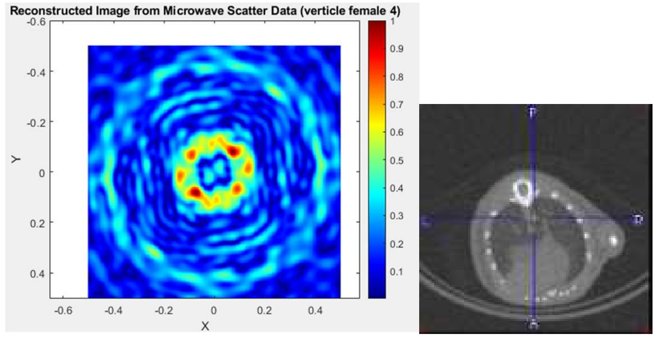

(a)

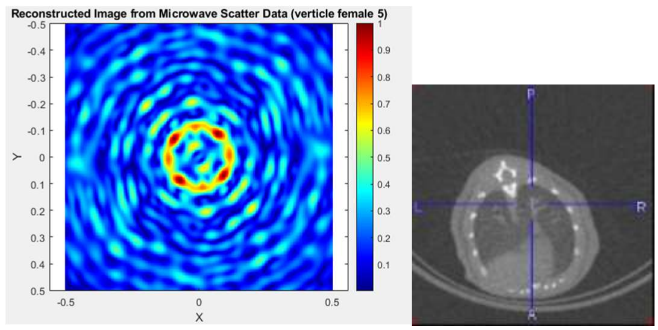

(b)

Figure 4.2.3.a: Microwave image reconstruction compared to corresponding CT scans: male #4, (b) male #5

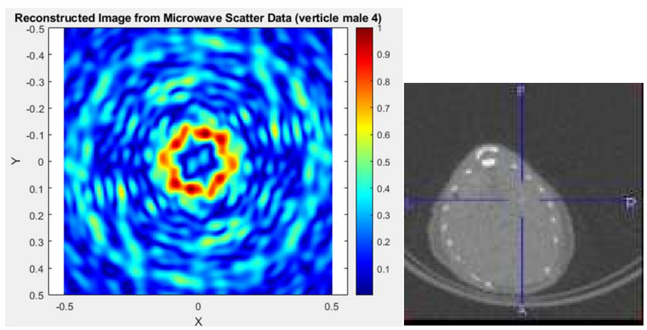

(a)

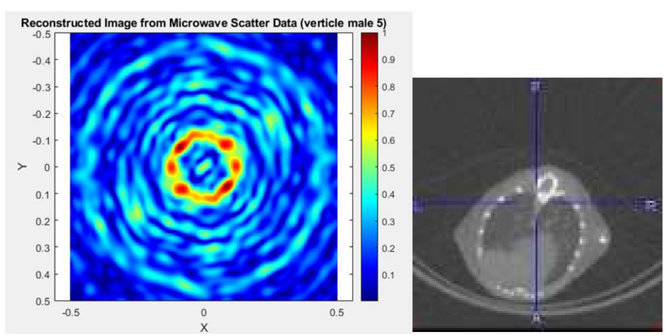

(b)

Figure 4.2.3.b: Microwave image reconstruction compared to corresponding CT scans: (a) female #4, (b) female #5

The microwave images capture the general locations and relative shapes of key features, but the resolution is noticeably lower than that of the CT scans as of now. For example, the boundaries of the lungs and liver in the microwave images appear more diffuse compared to the sharp delineation seen in the CT images. This difference is expected due to the inherent limitations of microwave imaging in spatial resolution, as it relies on dielectric property contrasts rather than density contrasts as in CT imaging.

Additionally, the microwave imaging highlights regions with distinct dielectric responses, such as the strong response around the thoracic area. This provides complementary information to the density-based contrasts of CT imaging, which is particularly valuable for applications that rely on material or tissue property differentiation. Despite the lower resolution, the microwave reconstructions demonstrate potential for non-invasive imaging, particularly when paired with other modalities like CT to enhance overall diagnostic capability.

Further optimization of the microwave reconstruction algorithm could improve spatial accuracy and boundary sharpness, making it a more effective tool for tissue characterization and localization.

4.3 Future work

Future work on improving microwave image reconstruction should focus on refining the underlying reconstruction algorithms. Advanced techniques like machine learning-based methods, can be explored to enhance resolution and image clarity.

Increasing the number of acquisition angles and optimizing the signal-to-noise ratio would result in more accurate reconstructions. Moreover, developing enhanced color mapping techniques can make the images visually intuitive, with better differentiation of tissues or regions with varying dielectric properties. Moreover, expanding from 2D slices to 3D image reconstruction could provide a more comprehensive view of the subject, making it easier to interpret anatomical structures.

Finally, developing user-friendly software tools is essential for researchers and clinicians to fully utilize these advancements. Interactive platforms that allow users to adjust reconstruction parameters, such as noise reduction or color schemes, would make the process more efficient.

Bibliography

[1] J.H. Scatliff and P.J. Morris. 'From Roentgen to magnetic resonance imaging: the history of medical imaging.' In: *North Carolina medical journal* 75.2 (2014), pp. 111–113. ISSN: 00292559.

[2] Massimo Guarnieri. 'The Early History of Radar'. In: 4 (Oct. 2010), pp. 36–42.

[3] Gaspare Galati. 'A Simultaneous Invention—The Former Developments'. In: *100 Years of Radar*. Cham: Springer International Publishing, 2016, pp. 55–77. ISBN: 978- 3-319-00584-3.

[4] Raquel. C Conceicao, Johan Jacob Mohr and Martin O'Halloran. *An Introduction to Microwave Imaging for Breast Cancer Detection*. eng. 2016.

[5] Mojtaba Fallahpour. 'Synthetic aperture radar-based techniques and reconfigurable antenna design for microwave imaging of layered structures'. In: (2013).

[6] S. Noghanian et al. *Microwave Tomography: Global Optimization, Parallelization and Performance Evaluation*. Springer New York, 2014. ISBN: 9781493907519.

[7] Serguei Semenov. 'Microwave Tomography: Review of the Progress Towards Clinical Applications'. In: *Philosophical Transactions: Mathematical, Physical and Engineering Sciences* 367.1900 (2009), pp. 3021–3042. ISSN: 1364503X.

[8] Serguei Y. Semenov and Douglas R. Corfield. *Microwave Tomography for Brain Imaging: Feasibility Assessment for Stroke Detection*. International Journal of Antennas and Propagation. 2008. (Visited on 12/10/2017).

[9] Vitaliy Zhurbenko. 'Challenges in the design of microwave imaging systems for breast cancer detection'. In: *Advances in Electrical and Computer Engineering* 11.1 (2011), pp. 91–96.

[10] D.H. Johnson and D.E. Dudgeon. *Array Signal Processing: Concepts and Techniques*. Prentice-Hall signal processing series. P T R Prentice Hall, 1993. ISBN: 9780130485137.

[11] Hamid Krim and Mats Viberg. 'Two decades of array signal processing research: the parametric approach'. In: IEEE signal processing magazine 13.4 (1996), pp. 67–94.

[12] Kim Mey Chew et al. 'Human brain microwave imaging signal processing: Frequency domain (s-parameters) to time domain conversion'. In: Engineering 5.05 (2013), p. 31.

[13] A. vander (André) Vorst. RF/microwave interaction with biological tissues. eng. Hoboken, N.J., 2006.

[14] System Reference document(SRdoc); Technical characteustics for SRD equipment using Ultra Wide Band Sensor Technology(UWB); medical, wellness and assisted living applications. ETSI, Mar. 2017.

[15] says:, P., says:, M. T., & says:, O. V. (2022, October 1). Radar Fundamentals (part I). Aircraft 101. https://basicsaboutaerodynamicsandavionics.wordpress.com/2016/04/12/rada

r-electronic-countermeasure/

[16] Facebook, N. (2022, April 27). Filtered backprojection (FBP) illustrated guide for Radiologic Technologists • How Radiology Works. How Radiology Works. https://howradiologyworks.com/filtered-backprojection-fbp-illustrated-guide-for-radiologic-technologists/

[17] says:, P., says:, M. T., & says:, O. V. (2022, October 1). Radar Fundamentals (part I). Aircraft 101. https://basicsaboutaerodynamicsandavionics.wordpress.com/2016/04/12/radar-electronic-countermeasure/

[18] Pu-ram polyurethane foam RF absorber. The EMC Shop. (n.d.). https://theemcshop.com/anechoic-chambers/emc-absorber/pu-ram-polyurethane-foam-rf-absorber-30-mhz-100-ghz/

[19] Elsheakh, D. N., & Abdallah, E. A. (2018, June 29). Ultra-wideband log periodic dipole antenna (LPDA) for wireless communication applications. SCIRP. https://www.scirp.org/journal/paperinformation?paperid=85767

[20] MegiQ. (n.d.). 6GHz 3-port vector network analyzer. https://www.megiq.com/products/vna-0460e

[21] Home - Humimic Medical. Humimic Medical -. (2023, February 22). https://humimic.com/

[22] Ozkan Katircioglu et al. 'Comparing ray tracing, free space path loss and logarithmic distance path loss models in success of indoor localization with RSSI'. eng. In: IEEE Publishing, Nov. 2011, pp. 313–316. ISBN: 9781457714993.

[23] D. J. (David J.) Daniels. *EM detection of concealed targets*. eng. Hoboken, N.J., 2010.

[24] M A Martin. Ultra Wideband Preliminaries. eng. Ed. by Boris Lembrikov. 2010.

Appendix A

Auto-Rotary Base codes

```
#include <Servo.h>
 Servo myServo;
 const int buttonPin = 2;  // Pin connected to the push button
 int lastButtonState = LOW;  // Variable to store the last button state
 int currentButtonState;  // Variable to store the current button state
 int motorSpeed = 90;  // Motor speed, 90 is stopped, 0 is full speed CCW, 180 is full speed
 clockwise

 void setup() {
  myServo.attach(9);  // Attach the servo to pin 9
  pinMode(buttonPin, INPUT_PULLUP);  // Set the button pin as an input with an internal pull-
 up resistor
  myServo.write(motorSpeed);  // Start with the motor stopped (neutral position)
 }
 void loop() {
  currentButtonState = digitalRead(buttonPin);  // Read the state of the button

  // Check if the button is pressed (LOW state) and if it was released before
  if (currentButtonState == LOW && lastButtonState == HIGH) {
    motorSpeed = motorSpeed + 5;  // Increment motor speed by 5 units

    // Ensure the motorSpeed value is within the valid range of 0-180
    if (motorSpeed > 180) {  // If speed exceeds 180, reset to neutral (90)
      motorSpeed = 90;  // Stop the motor
    }

    // Write the new motor speed to the servo
    myServo.write(motorSpeed);
    delay(200);  // Debounce delay to prevent multiple registrations from one press
  }

  lastButtonState = currentButtonState;  // Update the button state
 }
```

Appendix B

MATLAB Codes for Filter Back Projection Algorithm Testing

```
clear all
clc

% Sample image creation
img = zeros(256);
img(100:165, 100:156) = 255;

% Convert img to radon space
r_img = cRadon(img, 180);

% Reconstruction of the original image
bp_img = cFBP(r_img, 180);
ir_img = cART(r_img, 180, 1);

% Visualization
tiledlayout(1, 4)
nexttile
imshow(img)
title('Original image')

nexttile
imshow(r_img, [])
title('Converted to radon space')

nexttile
imshow(bp_img, [])
title('Filtered backprojection')

nexttile
imshow(ir_img, [])
title('Iterative reconstruction (1 iter.)')

% Function definitions
function sg = cRadon(img, theta)
    step = 1;
    angles = 1:step:theta;
    sg = zeros(size(img, 1), length(theta));

    for i = 1:length(angles)
        sg(:, i) = sum(imrotate(img, -angles(i), 'bilinear', 'crop'));
    end
end
```

```
function bp = cFBP(sg, theta)
    step = 1;
    angles = 1:step:theta;
    bp = zeros(length(sg));
    ramlak = abs(linspace(-1, 1, length(sg))');
    fft_R = fftshift(fft(sg, [], 1), 1);
    filtproj = ifftshift(fft_R .* ramlak, 1);
    sg = real(ifft(filtproj, [], 1));

    for i = 1:length(angles)
        tmp = repelem(sg(:, i), 1, length(sg));
        tmp = imrotate(tmp, angles(i), 'bilinear', 'crop');
        bp = bp + tmp;
    end
end

function ir = cART(sg, theta, niter)
    step = 1;
    angles = 1:step:theta;
    [ir, tdiff] = deal(zeros(length(sg)));

    for i = 1:niter
        for j = 1:length(angles)
            ir = imrotate(ir, step, 'bicubic', 'crop');
            tmp = sum(repelem(sg(:, j), 1, length(ir)), 2);
            diff = (tmp - sum(ir, 2)) / length(ir);
            for k = 1:length(ir)
                tdiff(:, k) = diff;
            end
            ir = ir + tdiff;
        end
    end
end
```

Appendix C

MATLAB Codes for Object Detection

```
% Clear workspace
clear;
clc;

%loading the data
path="1Data_collected\Square_PLA\" % the path that contains the data
csvFiles= dir(fullfile(path,"*.csv"));     % get all CSV files  (counter for number of angels
num_files=length(csvFiles);
for i = 1:num_files
   % read each CSV file for the current angle
   freq_data = readtable(sprintf("%s%d-VF.csv", path, (i-1)*10));

   ImS21(i,:) =freq_data.ImS21;
   ReS21(i, :) = freq_data.ReS21; % Assuming 'ReS21' column exists in the CSV
end

%define parameters
angles = 0:10:350; % angles from 0 to 360 degrees with a step of 10 degrees
freq_range = 0.4:0.02:4;    % frequency range from 0.4 GHz to 4 GHz in steps of 0.02 GHz(it can
be
num_freq = length(freq_range);
num_angles = length(angles);
S21_data = ReS21(:,:)+1i*ImS21(:,:); % a+bi complex

%2d grid for reconstruction (image resolution 500x500)
N = 500;  % resolution of the reconstructed image
x = linspace(-1, 1, N);
y = linspace(-1, 1, N);
[X, Y] = meshgrid(x, y);

%initialize the reconstructed image
% Initialize the reconstructed image
reconstructed_image = zeros(N, N);

%Iterate over each angle and perform back projection
for idx = 1:num_angles
   theta = angles(idx); % Current angle in degrees
   theta_rad = deg2rad(theta);

%s21 reading for the current angle
   s21_at_angle = S21_data(idx, :);

%apply ramp filter and Hann window in frequency domain
  filtered_s21 = filter_projection_hann(s21_at_angle, freq_range);

 % Back projection
   for i = 1:N
```

```
        for j = 1:N
            % Convert (X, Y) to rotated coordinates
            x_rot = X(i, j) * cos(theta_rad) + Y(i, j) * sin(theta_rad);

            % Find the corresponding frequency index
            [~, nearest_idx] = min(abs(freq_range - abs(x_rot)));

            % Back-project using complex S21 data
            reconstructed_image(i, j) = reconstructed_image(i, j) + ...
                real(filtered_s21(nearest_idx) * exp(1i * 2 * pi * freq_range(nearest_idx) * x_rot));
        end
    end
    fprintf('Processing angle %d of %d\n', idx, num_angles);
end

% Normalize the reconstructed image
reconstructed_image = reconstructed_image / num_angles;
threshold = 0.3 * max(reconstructed_image(:));  % 10% of the max value as threshold
reconstructed_image(reconstructed_image < threshold) = 0;


% display the reconstructed image
figure;
imagesc(x, y, reconstructed_image);
axis equal tight;
colormap('jet');
colorbar;
title('Reconstructed Image Using FBP with Hann Window Filtering');

%function to apply Hann window filter for filtered back-projection (FBP)
function filtered_proj = filter_projection_hann(s21_data, freq_range)
%perform FFT of the projection (real and imaginary components are included)
fft_data = fft(s21_data);
%create a Hann window filter in the frequency domain
hann_filter = hann(length(freq_range))';

 % Apply the Hann window to the FFT of the S21 data
filtered_fft = fft_data .* hann_filter;

    % Perform inverse FFT to obtain the filtered projection
    filtered_proj = ifft(filtered_fft);
end
```

Appendix D

MATLAB Codes for Animal Imaging

```
%% Data loading
path_empty = "1Data_collected/empty_strainer_hor";  % Empty chamber path
path_object = "1Data_collected/male4_15_21_ver/";  % Object chamber path

[S21_obj,freq,num_angles]=loadData(path_object,"ReS21","ImS21"); % Loading the object S21
angles = linspace(0, 360, num_angles);
angle_step = 360 / (num_angles - 1);
freq = freq * 1e9;
num_frequencies = length(freq);

empty = loadData(path_empty,"ReS21","ImS21"); % BaseLine
S21_cplx = S21_obj;
S21_obj = real(S21_obj) - real(empty);

%%define the output image grid (Cartesian Coordinates)
grid_size = 256; % Size of the reconstruction grid (256 x 256)
x = linspace(-0.5, 0.5, grid_size); % Define x coordinates
y = linspace(-0.5, 0.5, grid_size); % Define y coordinates
[X, Y] = meshgrid(x, y); % Create meshgrid for Cartesian grid

reconstruction = zeros(size(X)); % Initialize reconstruction grid

%over each angle and frequency to perform back-projection
for ang_idx = 1:num_angles
    angle = (ang_idx - 1) * angle_step; % Current angle in degrees
    for freq_idx = 1:num_frequencies
        frequency = freq(freq_idx);
        wavelength = 3e8 / frequency; % Calculate wavelength (c = 3e8 m/s)
        scatter_value = S21_obj( freq_idx,ang_idx); % Get scatter value

        %Wave number
        k = 2 * pi / wavelength;
        %back-projection without radial assumption
        phase_shift = exp(1j * k * (X * cosd(angle) + Y * sind(angle)));

        %reconstruction image by summing back-projection
        reconstruction = reconstruction + scatter_value * phase_shift;
    end
end

%%normalize the reconstructed image for visualization
```

```
reconstruction = abs(reconstruction); % Take the magnitude of the image
reconstruction = reconstruction / max(reconstruction(:)); % Normalize to [0, 1]

%display the reconstructed image
figure;
imagesc(x, y, reconstruction);
colormap('jet');
colorbar;
axis equal;
title('Reconstructed Image from Microwave Scatter Data (verticle male 5)');
xlabel('X');
ylabel('Y');
```

//Codes for loadData function

```
function [S_data,freq,num_angels] = loadData(path_object, real_column, imag_column)
% loadData loads complex scatter data from multiple CSV files.
%   path_object - path to the directory containing CSV files.
%   real_column - name of the column for the real part of S21 (e.g., 'ReS21').
%   imag_column - name of the column for the imaginary part of S21 (e.g., 'ImS21').

% Load CSV files from the specified directory
csvFiles = dir(fullfile(path_object, "*.csv"));
num_files = length(csvFiles);
ang_stp = 360 / (num_files - 1); % Calculate angle step

% Read the first file to get the number of frequency points
freq_data = readtable(fullfile(path_object, "0-VF.csv"), 'VariableNamingRule', 'preserve');
num_freq_points = height(freq_data);

% Initialize matrices for real and imaginary parts
ReS21_object = zeros(num_freq_points,num_files );
ImS21_object = zeros(num_freq_points,num_files );

% Load object measurements
for i = 1:num_files
    current_angle = ang_stp * (i - 1); % Calculate the angle for this file
    filename = fullfile(path_object, sprintf("%d-VF.csv", current_angle));
    freq_data = readtable(filename, 'VariableNamingRule', 'preserve'); % Read data from CSV file

    % Use specified column names to load real and imaginary parts
    ReS21_object(:, i) = freq_data.("ReS21");
    ImS21_object(:, i) = freq_data.("ImS21");
end

% Combine real and imaginary parts into complex data
S_data = complex(ReS21_object,ImS21_object);
freq=freq_data.(1);
num_angels=num_files;
end
```